View Article Online / Journal Homepage / Table of Contents for this issue
Dynamic Article Links

Molecular
BioSystems

Cite this: *Mol. BioSyst.*, 2012, **8**, 2605–2613

www.rsc.org/molecularbiosystems

PAPER

Differential RNAi screening provides insights into the rewiring of signalling networks during oxidative stress†‡

Mar Arias Garcia,§ Miguel Sanchez Alvarez,§ Heba Sailem, Vicky Bousgouni, Julia Sero and Chris Bakal*

Received 13th March 2012, Accepted 22nd June 2012
DOI: 10.1039/c2mb25092f

Reactive Oxygen Species (ROS) are a natural by-product of cellular growth and proliferation, and are required for fundamental processes such as protein-folding and signal transduction. However, ROS accumulation, and the onset of oxidative stress, can negatively impact cellular and genomic integrity. Signalling networks have evolved to respond to oxidative stress by engaging diverse enzymatic and non-enzymatic antioxidant mechanisms to restore redox homeostasis. The architecture of oxidative stress response networks during periods of normal growth, and how increased ROS levels dynamically reconfigure these networks are largely unknown. In order to gain insight into the structure of signalling networks that promote redox homeostasis we first performed genome-scale RNAi screens to identify novel suppressors of superoxide accumulation. We then infer relationships between redox regulators by hierarchical clustering of phenotypic signatures describing how gene inhibition affects superoxide levels, cellular viability, and morphology across different genetic backgrounds. Genes that cluster together are likely to act in the same signalling pathway/complex and thus make ''functional interactions''. Moreover we also calculate differential phenotypic signatures describing the difference in cellular phenotypes following RNAi between untreated cells and cells submitted to oxidative stress. Using both phenotypic signatures and differential signatures we construct a network model of functional interactions that occur between components of the redox homeostasis network, and how such interactions become rewired in the presence of oxidative stress. This network model predicts a functional interaction between the transcription factor Jun and the IRE1 kinase, which we validate in an orthogonal assay. We thus demonstrate the ability of systems-biology approaches to identify novel signalling events.

Introduction

Reactive Oxygen Species (ROS) such as oxygen anions, superoxide, hydroxyl radicals, and hydrogen peroxide are generated during normal growth and proliferation, as well as during an inflammatory response.[1–5] But the accumulation of ROS, either due to normal physiological processes or due to environmental factors, can lead to oxidative stress and detrimental effects on cellular constituents such as proteins, lipids, and DNA.[6] Organisms have thus evolved a number of diverse antioxidant mechanisms to reap the energetic and thermodynamic benefits of ROS-generating reactions such as oxidative phosphorylation and oxygen reduction during protein folding, while limiting ROS-induced damage. Glutathione, catalases, peroxidases, and superoxide dismutases (SODs) act directly to detoxify ROS;[5] while proteins such as TIGAR (TP53-induced glycolysis and apoptosis regulator)[7] and ErbB2[8] alter glycolytic flux to increase production of the antioxidant NADPH and thus indirectly affect ROS accumulation. Autophagy is also a key regulator of redox homeostasis by degrading ROS-producing mitochondria.[5]

Signalling networks that promote redox homeostasis are engaged by oxidative stress and in turn regulate transcription, translation, metabolism, and organelle morphogenesis. In many cell types, signalling network activity converges on the regulation of transcription factors (TFs) such as Nf-κB,[9–13] FOXO,[14–16] p53,[17] and Nrf-2.[18] However recent studies suggest that ROS levels are likely restrained by many different TFs and transcriptional programs,[19–23] which is perhaps not surprising given the fact that the levels of ROS can be affected through alterations in diverse cellular processes. But the architecture of signalling networks that regulate redox homeostasis is poorly understood.

Chester Beatty Laboratories, Division of Cancer Biology, Institute of Cancer Research, 237 Fulham Road, London, UK. E-mail: chris.bakal@icr.ac.uk

† Published as part of a themed issue dedicated to Emerging Investigators.

‡ Electronic supplementary information (ESI) available. See DOI: 10.1039/c2mb25092f

§ These authors contributed equally to this work.

Towards describing the signalling networks that respond to oxidative stress, we have developed an image-based readout of superoxide levels in single cells that can be used in the context of high-throughput RNAi screens. While screens for genes that regulate superoxide can provide lists of genes that contribute to redox homeostasis directly or indirectly, they do not by themselves provide insight into the architecture of networks that regulate ROS. One powerful means of inferring "functional interactions" – meaning interactions that occur between genes/proteins in signaling networks that control different cellular processes – is through the use of approaches that cluster genes based on multi-dimensional readouts of phenotype following gene inhibition.[24–28] Multi-dimensional readouts, or signatures, may be composed of different quantitative or qualitative measurements of cellular phenotypes following inhibition of a single gene.[24] For example we have previously used high-dimensional readouts of single cell morphology following RNAi to cluster genes into "local networks".[26] Alternatively multi-dimensional phenotypic signatures can be comprised of the same readout (*e.g.* viability) measured when the gene is inhibited across different genetic backgrounds;[29] as best typified by clustering of genetic interaction profiles following systematic double gene knockout in *S. cerevisiae*.[27] Here we gained insight into the architecture of networks which regulate redox homeostasis by clustering multi-dimensional phenotypic signatures that describe how inhibition of a single gene affects viability, cellular morphology, as well as superoxide levels in both unsensitised and sensitised genetic backgrounds. But as the cellular phenotypes and functional interactions following gene inhibition under normal conditions may not necessarily reflect those that occur in response to increased levels of ROS, we repeated our RNAi screens in cells with increased oxidative stress. By clustering "differential phenotypic signatures" which represent the difference in phenotypic signatures following gene inhibition in untreated and treated cells we can describe how signalling networks are rewired to promote redox homeostasis.

Results

To quantify cellular superoxide in the context of high-throughput image based screens we developed a novel method that uses dihydroethidium (DHE) to label cells. DHE is a blue-fluorescent cell permeable dye until it is oxidised by superoxide (O_2^-) to bright fluorescent red ethidium that intercalates within the cell's nuclear DNA (Fig. 1A).[30] Single cell superoxide levels can be quantified following image-acquisition of DHE-stained cells using image-processing algorithms. Briefly, the mean intensity of the oxidised-DHE/ethidium within the cell nucleus is normalised to the mean DAPI intensity within the same region. We validated our image-based assay by quantifying superoxide following chemical and genetic manipulations that

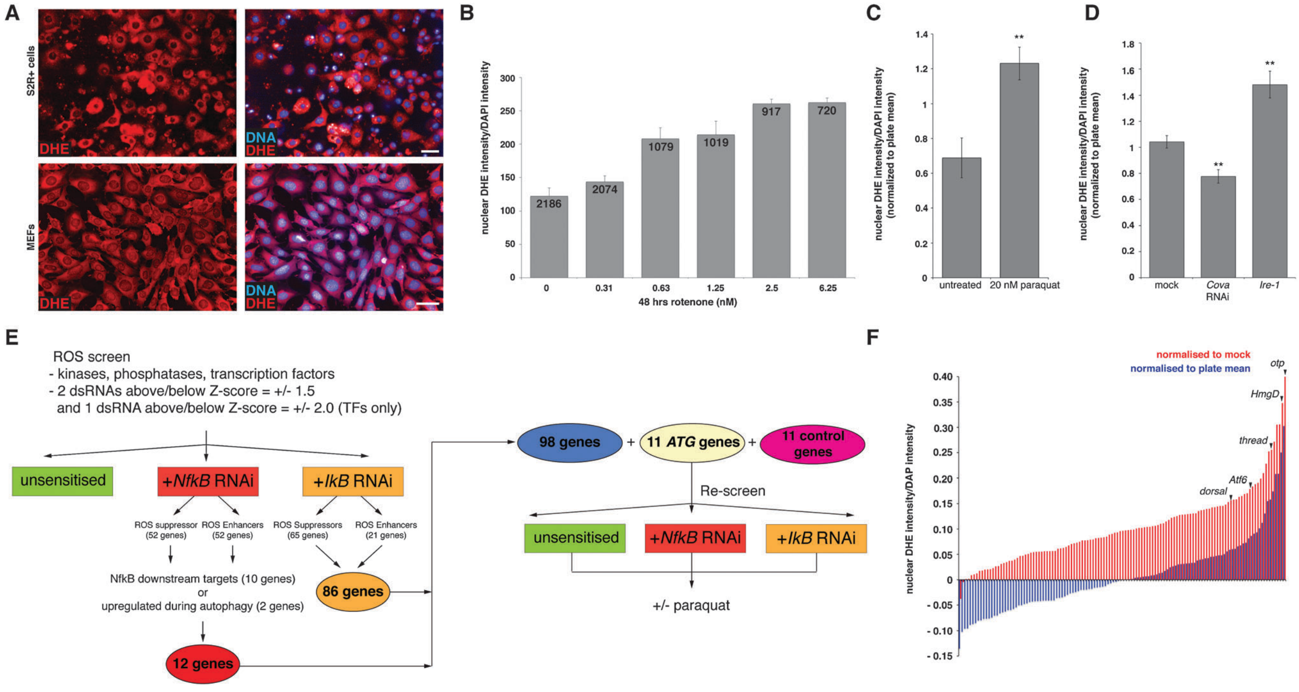

Fig. 1 An image-based assay for ROS levels. (A) *Drosophila* S2R+ or mouse embryonic fibroblasts (MEFs) cells stained with dihydroethidium (DHE) and DAPI. Scale bars are equal to 20 μm and 50 μm for images of S2R+ and MEFs respectively. (B) Nuclear DHE/DAPI ratio in MEFs quantified by image analysis of increasing doses of rotenone. Each column represents the mean of a population of single cells and is labeled with the number of cells that were analysed. (C) DHE/DAPI ratio (normalised to plate mean) of 384 untreated wells, or following addition of 1 mM paraquat for 18 h. (D) DHE/DAPI ratio ($n = 4$ wells, normalised to mock-treated cells) of mock-treated cells and cells incubated with RNAi targeting *Cova* and *IRE*1. (E) Flowchart describing initial screen for superoxide regulators and subsequent screen strategy. (F) DHE/DAPI ratio following gene inhibition (mean of experimental and technical replicates) for 120 genes and a mock-treated control in S2R+ cells. Red columns indicated values normalised to mock-treated cells, blue columns indicate values normalised to plate mean. Error bars represent standard error of the mean; ** $p < 0.01$ as compared to control sample determined by Student's *t*-test.

have been previously reported to alter the cellular redox state. Significant increases in superoxide levels are detected by microscopy in mouse embryonic fibroblasts (MEFs) following increasing doses of the mitochondrial poison rotenone (Fig. 1B) or in *Drosophila* S2R+ cells following 18 h incubation with 1 mM of the ROS-generating toxin paraquat (Fig. 1C). RNAi-mediated inhibition of *Cytochrome c oxidase subunit Va* (*Cova*) in *Drosophila* S2R+ cells leads to decreases in superoxide levels as previously reported[30] (Fig. 1D). These results validate our method as a means to quantify superoxide levels on a single-cell level.

Using this assay we performed a number of genome-scale RNAi screens of libraries targeting *Drosophila* kinases, phosphatases (the "KP set") and TFs ("the TF set") (Methods). We performed these screens in unsensitised genetic backgrounds and in cells where either the *Drosophila* Nf-κB gene *dorsal/dl*, or the *Drosophila* IκB gene *cactus* [31] was inhibited by RNAi (Fig. 1E). We screened Nf-κB and IkB deficient cells due to the highly conserved role of Nf-κB in the oxidative stress response.[13] IκB inhibits Nf-κB activity through cytoplasmic sequestration,[32] and degradation of IκB results in nuclear translocation and activation of Nf-κB.[33] Genes whose inhibition increases/decreases superoxide levels in *Nf-κB* or *IκB* deficient cells are presumably likely to play direct or indirect roles in Nf-κB-mediated regulation of superoxide. We consider genes as genuine regulators of superoxide levels if the weighted Z-scores (calculated based on the number of cells scored in replicate experiments) of two or more independent dsRNAs targeting the genes were above or below a threshold of 1.5 or -1.5 respectively (Fig. 1E). We also considered TFs to be regulators of superoxide if inhibition of at least 1 of 2 dsRNAs targeting a TF results in Z-scores above or below a threshold of 2.0 or -2.0 respectively. Because IκB opposes the effects of Nf-κB, it is highly unlikely that genes that enhance or suppress the effects of *Nf-κB* inhibition (*e.g.* increase ROS) would have identical effects in *IκB*-deficient cells. Thus we considered dsRNAs that induce similar phenotypes in both *Nf-κB*- and *IκB*-deficient cells to be false positives. Based on this intuition our false positive rate in these initial screens was estimated to be ~10%. Following the elimination of false-positives from our data, we identified 52 suppressors and 52 enhancers of superoxide levels in *Nf-κB*-deficient cells, and 65 suppressors and 21 enhancers of superoxide levels in *IκB*-deficient cells (Fig. 1E and Methods).

While these initial screens provide novel insight into the regulation of superoxide levels, we generated a new library of resynthesised dsRNAs targeting 120 genes based on these data for further validation and screening (Table S1, ESI‡). Because constitutive activation of Nf-κB, such as that which occurs following inhibition of IκB, is a hallmark of many diseases driven by inflammation,[1] this new library includes dsRNAs inhibiting 86 genes isolated in *IκB*-deficient screens. We also selected dsRNAs targeting *Dp*, *Dr*, *EcR*, *E*(*spl*), *eve*, *ftz*, *gcm*, and *gsb-n*, *Mef*2, and *oc* as these 10 genes were isolated by screening of *Nf-κB*-deficient cells, and are regulated by Dorsal/Nf-κB signaling.[34–36] Given the key role of autophagy in redox homeostasis we also included in the new library additional dsRNAs targeting 11 genes encoding components of the autophagy complex. Moreover we included dsRNAs inhibiting *CG16708* and *Ptpmeg* which were isolated as ROS suppressors in *Nf-κB* deficient cells and are transcriptionally upregulated during autophagy.[37] Finally we included in the library dsRNA targeting 11 control genes such as *Nf-κB*, *IκB*, the Nf-κB kinases *ik*-2, and *Kenny*, *Tor*, *Rac1*, and *Pbl/Ect-2*. Together our new library consists of dsRNAs targeting 120 genes.

As expected, inhibition of the vast majority of the 120 genes targeted in our new RNAi library increases superoxide levels, even in the absence of sensitizing cells with the addition of either *Nf-κB* or *IκB* RNAi (Fig. 1F, red columns). For example, inhibition of *IRE*1 and *ATF*6 increases superoxide levels (Fig. 1D and E). Both IRE1 and ATF6 are components of the Unfolded Protein Response (UPR) that is engaged by endoplasmic reticulum stress and concomitant with an elevation in ROS levels.[38,39] Thus inhibition of these proteins may result in unresolved ER stress and accumulation of superoxide. But undoubtedly these genes we have identified in this screen suppress ROS levels through a variety of means.

We next sought to determine how these 120 genes functionally interact in cellular systems. As single values following RNAi knockdown are not appropriate to gain insight into functional interactions, we used different means to increase the dimensionality of our phenotypic signatures through subsequent rescreening in S2R+ cells. Specifically we quantified: (1) cell size and cell roundness following RNAi; (2) the effect of gene inhibition on viability; (3) superoxide levels, morphology, and viability following RNAi mediated inhibition of either *Nf-κB* or *IκB*. Two independent dsRNAs were used to target each gene, each designed to have no or few (<10) off-target effects (OTEs), and each dsRNA was screened 4 or 8 different times in the same experiment. The mean score of all technical and experimental repeats was then used to generate the final phenotypic signature. Notably, for assays described in this work, we calculated a Z-score using the mean score of all wells screened for a specific assay (*e.g.* a particular measurement in a certain genetic background), thus genes will have both positive and negative Z-scores for DHE/DAPI ratios (Fig. 1F, blue columns) even though many are suppressors of superoxide levels when compared to mock-treated S2R+ cells (Fig. 1F, red columns).

We assigned groups of genes into different "phenoclusters" of functional interactions using hierarchical clustering and cluster validation. Groups of genes are considered to be a phenocluster if the confidence in the existence of the cluster is $p \leq 0.05$, where the p-value is calculated by multi-scale bootstrap resampling (Methods). In the screen of cells grown under normal conditions, we identified 13 validated phenoclusters (Fig. 2 and Fig. S1 (ESI‡)). Although many of the genes in this dataset are very poorly characterized, we identified some cases where clustering recapitulated previously known biochemical interactions. For example 6/8 and 3/3 genes in two different clusters are ATG genes. This clustering is driven by the fact that while inhibition of these genes affects morphology in *dorsal/Nf-κB*-deficient cells, the effects are otherwise relatively mild (Fig. 2). Thus we conclude that in *Drosophila* cells growing under normal conditions, inhibition of autophagy does not greatly impact cellular phenotypes. Presumably, this is in part due to the fact that autophagy is dispensable for growth and viability when cells are grown in rich media, and

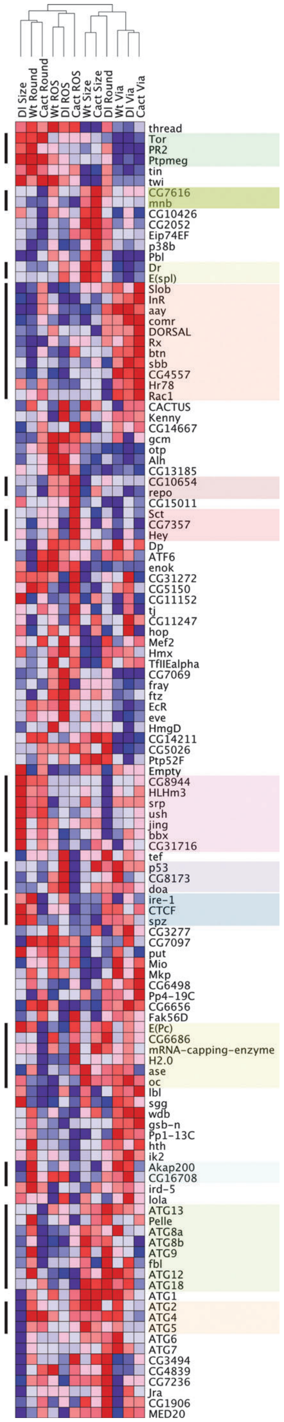

Fig. 2 Clustering of phenotypic signatures following RNAi-mediated inhibition of 121 genes. Viability (*via*), cell area (size), roundness (round), and superoxide levels (ROS) were quantified in *Drosophila* cells following RNAi-mediated inhibition in unsensitised cells (wt), or in sensitised genetic backgrounds where either *dorsal*/*Nf-κB* (*dl*) or *cactus*/*IκB* (*cact*) were also targeted by RNAi. All phenotypic scores are normalised by converting the raw score into *Z*-scores. The heat map is generated by converting *Z*-scores to colors using the mean, minimum, and maximum values in each row. Red coloring indicates relatively high *Z*-scores, blue coloring indicates relatively low *Z*-scores. Complete linkage clustering was performed using a city-block distance metric. Only clusters which are considered to be of high-confidence (p-value $\leq$ 0.05) following resampling are highlighted (black bars and coloured shading).

proteins such as Tor are actively repressing the induction of autophagy.[40,41] We also note that *Srp* and its target *ush* are part of the same cluster.[42] Notably there are several potential interactions between genes in this dataset that are not observed. For example, Mef2 is known to regulate the transcription of many genes in this dataset including *ase*, *HLHm3*, *lbl*, *lola*, *Dp*, *hth*, *E(spl)*, *eve*, *hth*, *ush*, *TFIIalpha*, and *fray*[36] during embryonic development, but only *Dp* and *E(spl)* cluster with each other (Fig. 2). The fact that we do not observe previously established functional interactions likely reflects the highly dynamic nature of these interactions. For example Mef2 may upregulate many of its known downstream targets only during embryogenesis, but not in proliferating S2R+ cells.

To determine how rewiring of cellular networks occurs in response to oxidative stress, we repeated all screens following incubation of cells with 1 mM paraquat. Scores of each phenotypic assay performed on untreated cells were then subtracted from comparable scores generated from screening of cells in oxidative stress to generate differential phenotypic signatures.[43,44] The largest change in cellular superoxide levels between untreated and paraquat-treated cells was observed following inhibition of the phosphatase-encoding gene *alphabet* (Fig. 3) which is remarkably consistent with the role of this gene in participating in the stress response *in vivo*.[45] Inhibition of *Atg7*, *Atg8a*, *Atg8b*, *Atg9* leads to increases in superoxide levels in paraquat-treated but not untreated cells supporting the notion that autophagy is a critical suppressor of ROS in periods of oxidative stress.[46] Targeting of Nf-κB signalling components *ird-5*, and *pelle*/*IRAK* by RNAi also increases superoxide levels in the presence of paraquat compared to control cells, consistent with the well-established role of Nf-κB signalling in the response to oxidative stress.[13] Interestingly, inhibition of *tin* and its transcriptional targets *E(spl)* and *Dr*[36] mimicked the effects of autophagy suggesting a novel function for Tin signalling. Finally inhibition of *IRE1*, but not *ATF6*, results in even higher levels of ROS compared to the experimental mean following treatment with paraquat resulting in a high positive differential DHE/DAPI *Z*-score (Fig. 3). Thus although both IRE1 and ATF6 are canonical components of the UPR, only IRE1 contributes to ROS suppression during periods of oxidative stress.

We reasoned that if the knockdown of two genes results in similar differential phenotypic signatures, they functionally interact during the oxidative stress response. Thus we clustered the differential signatures and identified high-confidence clusters ($p \leq 0.1$) through multi-scale bootstrap resampling. We identified 161 functional interactions, 138 that are unique to cells exposed to oxidative stress (Fig. S1, ESI‡). We then generated a network of interactions where different genes are nodes, and edges describe that two genes belong to a similar phenocluster following screening under normal conditions (Fig. 4, blue edges), or following differential analysis (Fig. 4, red edges). When two genes belong to the same cluster under both untreated conditions and following differential analysis this is denoted by a black edge. Thus this graph describes how interactions between key genes in the redox homeostasis network become rewired during periods of oxidative stress.

Perhaps most strikingly through differential analysis we observed extensive rewiring of functional interactions amongst

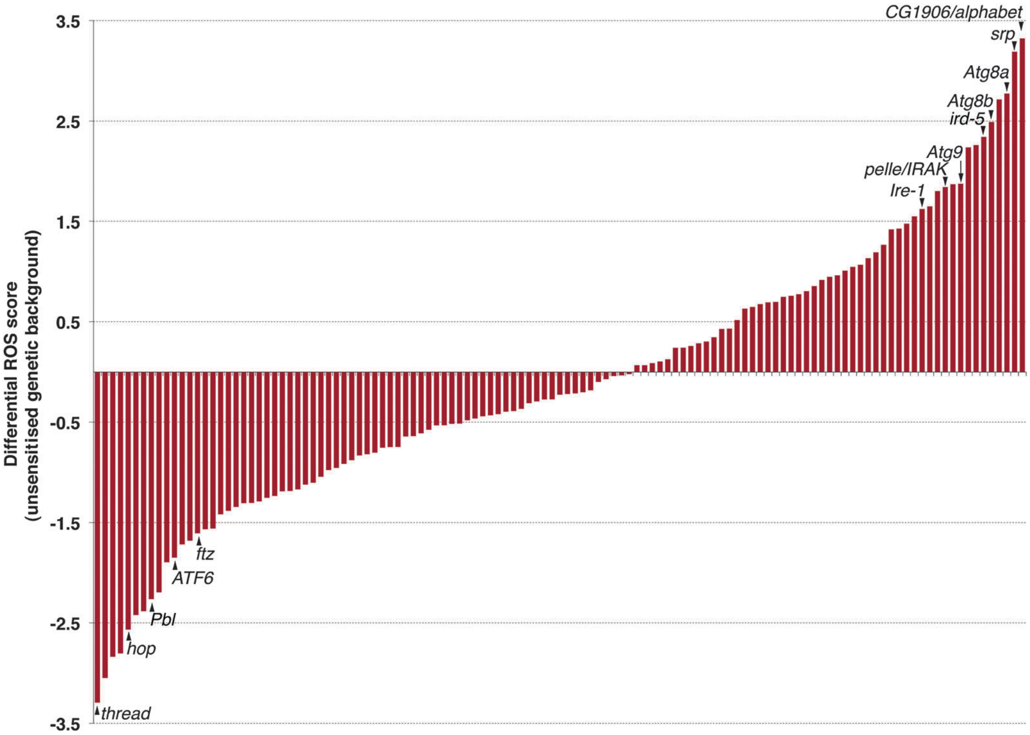

Fig. 3 Difference in superoxide levels in paraquat-treated *versus* untreated cells. Genes are ordered on the *x*-axis based on the difference in their Z-score describing superoxide levels in paraquat-treated cells *versus* untreated cells (low to high).

ATG genes in response to oxidative stress. For example, many of the functional interactions observed following screening and clustering in untreated cells were not observed by differential analysis. Rather 5/12 ATG genes were part of two new clusters. The differential phenotypic signatures of *Atg1*, *Atg2* and *Atg6* cluster with that of *p53*, consistent with the role of *Drosophil*a p53 in promoting autophagy during starvation.[47] Moreover, the clustering of *Atg4* and *Atg5* with the ecdysone receptor (*EcR*) is consistent with EcR's ability to upregulate autophagy upon activation.[48] Potentially the diverse effects of inhibiting different *Atg* components reflect disruption of the autophagic process at different stages (*e.g.* Atg1 mediated initiation *vs.* maturation).[46]

We next sought to further validate whether our systems-driven analysis of the oxidative stress response has a predictive value. Given that our data suggest a unique role for IRE1 in promoting redox homeostasis (Fig. 3), interactions with *IRE*1 are of particular interest. Activation of IRE1 leads to activation of its RNAse domain, sequence-specific endoribonucleolytic cleavage, and subsequent splicing of *xbp*1 mRNA, leading to the removal of a stop codon normally present in the 5′-end of *xbp*1 mRNA; which permits the translation of full-length Xbp1 protein.[49] IRE1 can also phosphorylate and activate Jun N-terminal kinase (JNK).[50] While under transient stress, IRE1 promotes survival, chronic IRE1 activity leads to cell death.[51] But how IRE1 is regulated, and how its output is tailored (*e.g.* to promote survival *vs.* death) are still unclear. Our network model predicts that *Drosophila Jun* makes a unique interaction with *IRE*1 (Fig. 4) during periods of oxidative stress, and thus we sought to test the effects of *Jun* inhibition on IRE1 activation.

In order to test the effect of gene inhibition on IRE1 activity, we monitored the IRE1-dependent splicing of endogenous *xbp-1* mRNA following exposure of cells to the glycosylation inhibitor tunicamycin; which induces ER stress and activation of IRE1.[49] We quantified *xbp*1 splicing in tunicamycin *versus* paraquat, as tunicamycin is expected to be a much more specific activator of IRE1. Inhibition of *IRE*1 by RNAi effectively prevents *xbp*1 splicing following tunicamycin treatment (Fig. 5). Targeting of *Jun* by RNAi also results in significant decreases in splicing of *xbp*1 mRNA (Fig. 5) following engagement of the UPR by tunicamycin. Taken together this finding validates the use of differential screening to identify novel interactions that occur uniquely in response to specific stimuli. Moreover, this suggests that Jun is required for maximal activation of *IRE*1.

Conclusions

The main contribution of this study is the description of novel functional interactions between genes that occur in response to oxidative stress. The fact that functional interactions can be experimentally validated demonstrates that differential analysis of multidimensional phenotypic signatures generated using a combination of readouts across diverse genetic backgrounds is a useful means by which to describe signalling networks. This work is a natural extension of recent studies of differential genetic interactions in yeast.[44]

Critically, while we have provided insight into the connectivity between genes/proteins, how inhibition of many of these genes affects superoxide levels is still unclear. We have shown that autophagy does not play a major role in regulating superoxide levels in rich media. Interestingly, the UPR appears to play an

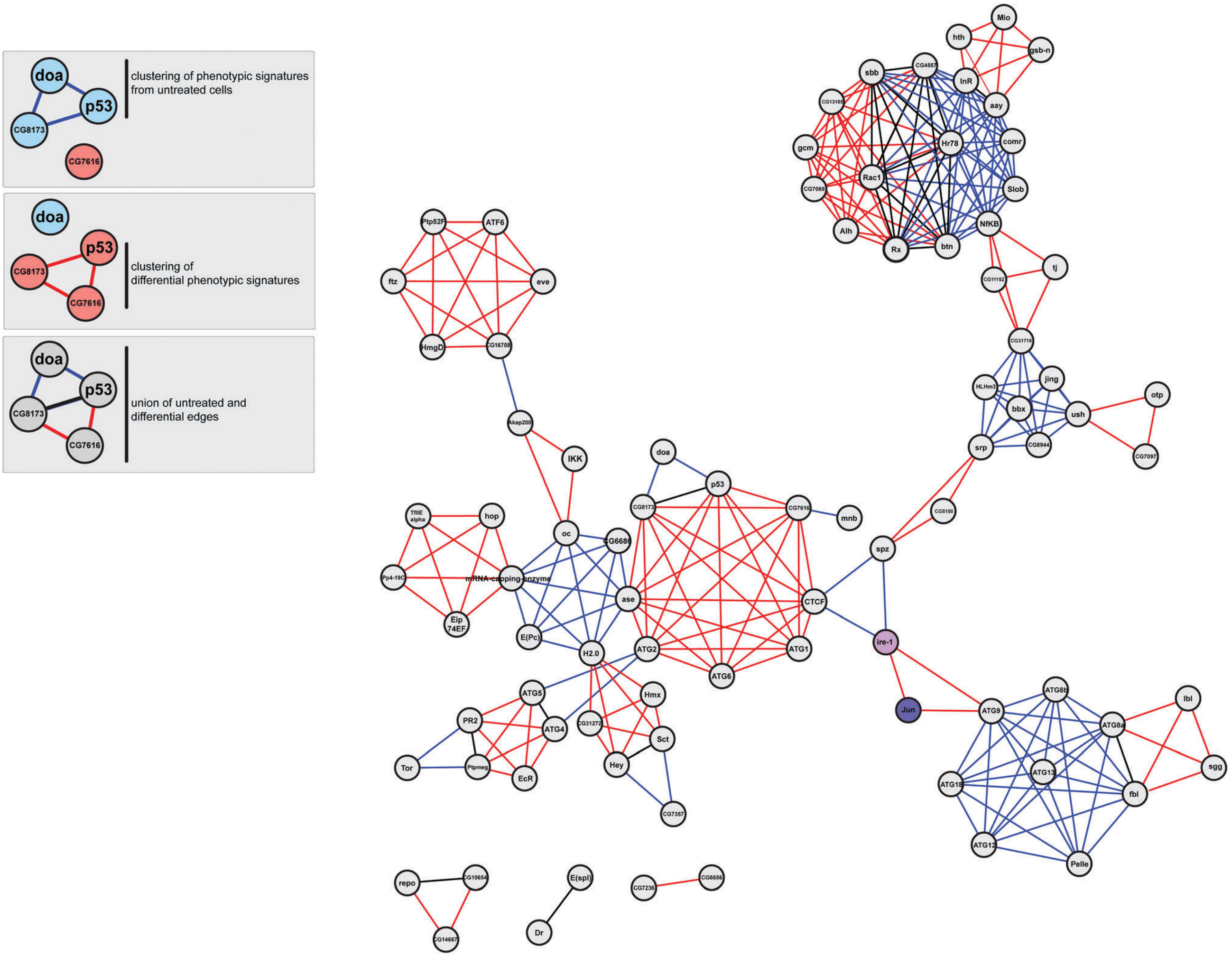
doa
p53
CG8173
CG7616
clustering of phenotypic signatures from untreated cells
clustering of differential phenotypic signatures
union of untreated and differential edges
Mio
hth
gsb-n
sbb
InR
aay
gcm
Hr78
comr
Rac1
Slob
NfKB
Alh
Rx
btn
tj
Ptp52F
ATF6
ftz
eve
HmgD
Akap200
IKK
doa
p53
CG8173
CG7616
mnb
hop
oc
mRNA-capping-enzyme
ase
CTCF
spz
E(Pc)
H2.0
ATG2
ATG1
ATG6
ire-1
Jun
ATG9
ATG8b
ATG8a
lbl
sgg
ATG5
PR2
ATG4
Hmx
Sct
Hey
Tor
Ptpmeg
EcR
ATG18
ATG13
fbl
ATG12
Pelle
jing
bbx
ush
otp
srp
repo
E(spl)
Dr

Fig. 4 Network-based interpretation of the rewiring of functional interactions during oxidative stress. Each node is a gene that was screened in both untreated and paraquat-treated cells. Blue edges denote that the genes belong to the same validated cluster following clustering of untreated phenotypic signatures. Red edges denote that belonging to the same validated cluster following clustering of differential phenotypic signatures. Black edges denote the genes are part of the same clustering following screening in untreated cells and differential analysis. IRE1 and Jun are highlighted in light purple. Nf-κB signalling components Kenny, Spz, and Nf-κB are highlighted in red.

important role in redox homeostasis during periods of normal growth and proliferation, which is consistent with the idea that ER and redox homeostasis must be tightly coordinated.[52] The UPR is thought of as acting through three different branches, which are activated by IRE1, ATF6, and PERK respectively.[53,54] Each branch regulates both specific and overlapping downstream processes that promote homeostasis. Interestingly in our initial screen for regulators of superoxide we did not isolate PERK, and inhibition of ATF6 did not affect superoxide levels in response to paraquat. Thus it is possible that while all three branches of the UPR are activated by classical ER stress (*e.g.* the accumulation of unfolded protein), the IRE1 branch is specific to oxidative stress. Although a model whereby IRE1 is specifically activated by oxidative stress is complicated by the fact that oxidative stress can inhibit folding.[38,55] Further screening under diverse conditions that activate the UPR in combination with the analysis methods described in this work may shed light onto the specific activation of different UPR branches.

In the course of these studies we demonstrate the usefulness of systems-driven methods in identifying novel signalling events. Specifically, we made the prediction that the TF Jun is a regulator of IRE1 activity, which we validate by showing that the *Jun* inhibition significantly decreases the splicing of *xbp*1 *mRNA* during periods of ER stress. IRE1 can promote Jun-mediated transcription through phosphorylation and activation of JNK,[50] but regulation of the IRE1-Xbp1 axis by Jun has not been previously observed. While IRE1 activation is largely mediated directly by unfolded proteins and/or disengagement of ER chaperones,[50] and it is not yet clear as to how Jun may be involved in regulating IRE1 mediated splicing of *xbp1*. This finding could potentially have a number of important implications as it suggests that full activation of the IRE1 may require additional signalling inputs in addition to unfolded proteins, and/or that Jun could be part of a positive feedback loop which sustains IRE1 activity.

Methods summary

Cell culturing and dsRNA experiments

Drosophila S2R+ cells were cultured in Schneider's insect media (Sigma), 10% fetal bovine serum (Sigma), and

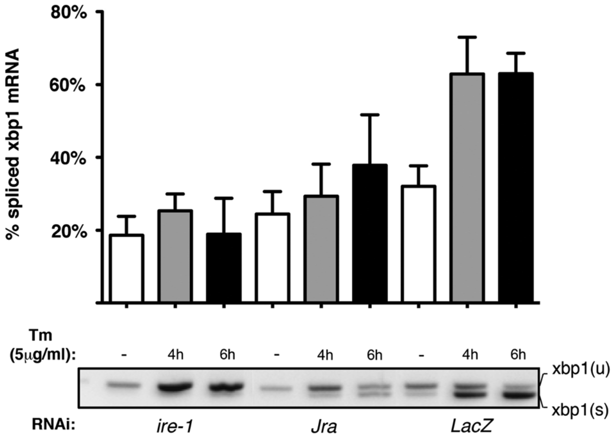

Fig. 5 Validation of a novel functional interaction identified in our screen. Cells were transfected with the indicated dsRNAs and then either mock-treated with DMSO or treated for the indicated times with 5 μg ml^{-1} of tunicamycin. Total RNA was purified and RT-PCR analysis for splicing of endogenous xbp1 mRNA was performed. xbp1(u): unspliced xbp1 mRNA species; xbp1(s): spliced xbp1 mRNA species. Error bars represent standard error of the mean from three replicate analyses.

penicillin–streptomycin (Gibco). All dsRNA experiments were performed using the bathing protocol as described by Ramadan *et al.*[52] Mouse Embryonic Fibroblasts (MEFs) were cultured in Dubelcco's modified Eagle's F-12 medium, 10% fetal bovine serum (Sigma), and penicillin–streptomycin (Gibco).

ROS assay

Staining for superoxide was done as described by Owusu-Ansah *et al.*[30] Briefly, live cells were incubated in the presence of 15 μM dihydroethidium (DHE) for 15 minutes, washed twice in media, fixed in 4% paraformaldehyde/0.1% Triton X-100 for 10 minutes, washed once in phosphate buffered saline (PBS), incubated with 4′,6-diamidino-2-phenylindole (DAPI) in PBS for 5 minutes, and then washed in PBS. Paraquat was added to the cells 18 h prior to staining/fixation, and rotenone was added to cells for 48 h prior to staining/fixation.

High-throughput automated image analysis

To calculate the effects of individual dsRNAs ROS levels in a high-throughput manner, we imaged cells using a PerkinElmer Opera Microscope using a 60× water immersed objective using a 405 laser to excite both the DHE and DAPI labels. 450/50 and 600/40 emission filters were used to capture the DAPI/DHE signal and oxidised-DHE (ethidium) signal respectively. We imaged 20–35 sites per well. MEFs were imaged using a 20× air objective. Following imaging, we first quantified ROS levels by implementing an algorithm *via* the Columbus interface (PerkinElmer) that: (1) uses the DAPI signal (present in all cells) to identify individual cells, detects nuclear edges, and then calculates nuclear area (in pixels); (2) identifies cellular boundaries by DHE staining and then calculates cell area and roundness; (3) calculates the mean ethidium and mean DAPI signal intensity in nucleus (individual pixel intensity can range from 0 to 4095 total cell area for each cell); (3) calculates a ratio of nuclear DHE/DAPI; (4) repeats steps 1 through 3 for each field; (4) exports a mean value DHE/DAPI intensity, cell area, and roundness for all cells in every well. Typically 200–1000 cells are imaged per well.

Initial screens for regulators of superoxide

Genes contributing to superoxide homeostasis were first isolated in genome-scale screens of the KP and TF sets (described in detail at www.flyrnai.org). In these initial screens *Drosophila* BG-3 cells were used. Unless otherwise denoted, all RNAi experiments were performed four days after treatment with dsRNA. All dsRNAs described in this study have been designed to have zero, or extremely few off-target effects (OTEs). The KP set targets *Drosophila* genes that encode proteins for kinases or phosphatases. Approximately three amplicons per gene target 563 genes over 8 assay plates. Unique dsRNAs targeting both kinase and phosphatase genes are distributed randomly on all eight plates. The TF sub-library targets the complete set of Drosophila genes that encode transcription factors as well as other DNA binding proteins and nuclear factors. Approximately two amplicons per gene target 993 genes over 9 assay plates. For combinatorial experiments we added a second dsRNA to the cells in suspension prior to plating. The second dsRNA was diluted such that cells in each well were incubated with an additional 0.25 μg of dsRNA. Because the KP and TF sets are designed differently, with many more dsRNAs being tested per gene in the KP set, screens in each set are scored differently. In unsensitised and sensitised KP screens a gene is considered to be a potential regulator of ROS if two independent dsRNAs targeting that gene scores above a *Z*-score of 1.5, or below a *Z*-score of −1.5. In the case of TF screens, a gene is considered to be a potential regulator of ROS if a single dsRNA targeting that gene results in a ROS *Z*-score of above 2.0, or below −2.0. In cases where 2 or more independent dsRNAs resulted in significant but uncorrelated effects on ROS levels (*e.g.* a dsRNA targeting a gene results in *Z*-score >2.0 whereas another results in a score <-2.0), they were eliminated from our hit list. Other genes were considered to be false positives if their inhibition had similar effects on ROS levels in both *Nf-κB-* and *IκB*-deficient backgrounds, which would be unexpected based on the fact that IκB inhibits Nf-κB activity.

Targeted RNAi screens for ROS and viability

The 120 genes described in this study were targeted by 2–3 independent dsRNAs arrayed in a random pattern across two 384-well plates. On each plate, an individual dsRNA is scored in either 2 or 4 replicates. Each screen (ROS/shape in untreated cells, ROS/shape in paraquat treated cells) including all double RNAi conditions was performed in individual batches. Each plate was screened in duplicate. The viability screen was performed in a similar manner except that all experiments were performed in the same batch.

Viability assays

The CellTiter-Glo Luminescent Cell Viability Assay Kit (Promega) were used to monitor cell viability following the manufacturer's instructions.

Z-Score calculations and differential analysis

Each screen was performed in duplicate, and the weighted mean DHE/DAPI ratio, cell area, and roundness scores of replicate wells were calculated using the number of cells analysed in each well. For viability scores, the mean of replicate plates was calculated. A *Z*-score for each feature (area, roundness, DHE/DAPI ratio, viability) for each well mean was then calculated by subtracting the mean score of all wells on all replicate plates in a screen, from the individual well mean, and dividing by the standard deviation of the replicate plates. *Z* is the distance between the weighted mean sample score and the plate mean in units of the standard deviation. *Z* is negative when the raw score is below the mean, positive when above. For each gene the *Z*-scores of all wells with dsRNAs targeting that gene (both experimental and technical replicates) were averaged to generate final phenotypic signatures. To calculate a differential phenotypic signature, the *Z*-scores that make up signatures of untreated cells were subtracted from *Z*-scores that make up the signatures of paraquat treated cells.

Hierarchical clustering

All clustering was performed using Cluster 3.0 (Michiel de Hoon, Seiya Imoto, Satoru Miyano), which is based on Cluster (Michel Eisen, University of California, Berkeley). Clustering was performed by the complete linkage methods using city-block distance as the similarity metric. All clustering graphs were generated using GenePattern (Broad Institute of Harvard and MIT).

Cluster validation

The Pvclust package was used in **R** to validate the existence of different clusters. Different *p*-values were calculated *via* multi-scale bootstrap resampling. For phenotypic signatures derived following screening of untreated cells, a *p*-value of ≤ 0.5 was used as a cut-off to determine validated clusters. For clustering of differential signatures a *p*-value of ≤ 0.1 was used as a cut-off to determine validated clusters.

Network generation

The Cytoscape package (www.cytoscape.org) was used to plot a network of functional interactions.

Xbp1 splicing assay

The splicing of endogeneous *Drosophila xbp*1 was determined by RT-PCR using primer sets that detect both the unspliced and spliced forms of *xbp*1. The dsRNAs used against *IRE*1 and *Jun* in the experiment were DRSC15606 and DRSC07447, respectively. Mock- or RNAi-treated S2R+ cells were exposed to 5 mg ml^{-1} tunicamycin for 0, 4 and 6 h prior to lysis by the Trizol reagent. cDNA was prepared using MMLuV standard reagents and random hexamers as recommended by the supplier (Invitrogen). PCR for assessing IRE1-dependent unconventional splicing of endogenous xbp1 was performed using the oligonucleotide pair **F**: CAGATGCATCAGCCAATCCA and **R**: CACAACTTTCCAGAGTGAG with the Taq MasterMix DNA polymerase kit (Qiagen), using 29 cycles and an annealing temperature of 53 °C. PCR products were resolved in 2% TBE–agarose gels, UV-imaged in a BioDocIt imaging station (UVP) under unsaturated conditions and quantified using the Quantity One BioRad open software. The splicing ratio of xbp1 is calculated as [xbp1(s)/xbp1(s) + xbp1(u)] × 100.

Dorsal/*Nf-κB* and *cactus*/*IκB* dsRNAs

For combinatorial screens and expression profiling experiments we used DRSC29023 to inhibit *dorsal*/*Nf-κB* and DRSC3501 to target *cactus*/*IκB*.

Acknowledgements

This work was funded by the Biotechnology and Biological Sciences Research Council (BB/I002510/1). We are indebted to Alexis Barr and Louise Evans for assistance with revising the manuscript. We also thank the Drosophila RNAi Screening Center at Harvard Medical School, and in particular Stephanie Mohr, Quentin Gilly, Benjamin McElvany and Matt Booker for assistance in performing RNAi screens. C.B. is a Research Career Development Fellow of the Wellcome Trust.

References

1 S. I. Grivennikov, F. R. Greten and M. Karin, *Cell (Cambridge, Mass.)*, 2010, **140**, 883–899.
2 R. B. Hamanaka and N. S. Chandel, *Curr. Opin. Cell Biol.*, 2009, **21**, 894–899.
3 E. A. Veal, A. M. Day and B. A. Morgan, *Mol. Cell*, 2007, **26**, 1–14.
4 K. E. Wellen and C. B. Thompson, *Mol. Cell*, 2010, **40**, 323–332.
5 R. Scherz-Shouval and Z. Elazar, *Trends Biochem. Sci.*, 2011, **36**, 30–38.
6 T. Finkel, *Nat. Rev. Mol. Cell Biol.*, 2005, **6**, 971–976.
7 K. Bensaad, A. Tsuruta, M. A. Selak, M. N. Vidal, K. Nakano, R. Bartrons, E. Gottlieb and K. H. Vousden, *Cell (Cambridge, Mass.)*, 2006, **126**, 107–120.
8 Z. T. Schafer, A. R. Grassian, L. Song, Z. Jiang, Z. Gerhart-Hines, H. Y. Irie, S. Gao, P. Puigserver and J. S. Brugge, *Nature*, 2009, **461**, 109–113.
9 H. Kamata, S. Honda, S. Maeda, L. Chang, H. Hirata and M. Karin, *Cell (Cambridge, Mass.)*, 2005, **120**, 649–661.
10 K. Maehara, T. Hasegawa and K. I. Isobe, *J. Cell. Biochem.*, 2000, **77**, 474–486.
11 R. Mathew, C. M. Karp, B. Beaudoin, N. Vuong, G. Chen, H. Y. Chen, K. Bray, A. Reddy, G. Bhanot, C. Gelinas, R. S. Dipaola, V. Karantza-Wadsworth and E. White, *Cell (Cambridge, Mass.)*, 2009, **137**, 1062–1075.
12 C. G. Pham, C. Bubici, F. Zazzeroni, S. Papa, J. Jones, K. Alvarez, S. Jayawardena, E. De Smaele, R. Cong, C. Beaumont, F. M. Torti, S. V. Torti and G. Franzoso, *Cell (Cambridge, Mass.)*, 2004, **119**, 529–542.
13 M. J. Morgan and Z. G. Liu, *Cell Res.*, 2011, **21**, 103–115.
14 M. C. Wang, D. Bohmann and H. Jasper, *Cell (Cambridge, Mass.)*, 2005, **121**, 115–125.
15 Z. Tothova and D. G. Gilliland, *Cell Stem Cell*, 2009, **4**, 196–197.
16 Z. Tothova, R. Kollipara, B. J. Huntly, B. H. Lee, D. H. Castrillon, D. E. Cullen, E. P. McDowell, S. Lazo-Kallanian, I. R. Williams, C. Sears, S. A. Armstrong, E. Passegue, R. A. DePinho and D. G. Gilliland, *Cell (Cambridge, Mass.)*, 2007, **128**, 325–339.
17 I. A. Olovnikov, J. E. Kravchenko and P. M. Chumakov, *Semin. Cancer Biol.*, 2009, **19**, 32–41.
18 G. P. Sykiotis and D. Bohmann, *Sci. Signaling*, 2010, **3**, re3.
19 A. Vrailas-Mortimer, T. del Rivero, S. Mukherjee, S. Nag, A. Gaitanidis, D. Kadas, C. Consoulas, A. Duttaroy and S. Sanyal, *Dev. Cell*, 2011, **21**, 783–795.
20 P. Horak, A. R. Crawford, D. D. Vadysirisack, Z. M. Nash, M. P. DeYoung, D. Sgroi and L. W. Ellisen, *Proc. Natl. Acad. Sci. U. S. A.*, 2010, **107**, 4675–4680.
21 N. Sen, Y. K. Satija and S. Das, *Mol. Cell*, 2011, **44**, 621–634.

22 A. Avivar-Valderas, E. Salas, E. Bobrovnikova-Marjon, J. A. Diehl, C. Nagi, J. Debnath and J. A. Aguirre-Ghiso, *Mol. Cell. Biol.*, 2011, **31**, 3616–3629.
23 B. Vurusaner, G. Poli and H. Basaga, *Free Radicals Biol. Med.*, 2012, **52**, 7–18.
24 B. Sonnichsen, L. B. Koski, A. Walsh, P. Marschall, B. Neumann, M. Brehm, A. M. Alleaume, J. Artelt, P. Bettencourt, E. Cassin, M. Hewitson, C. Holz, M. Khan, S. Lazik, C. Martin, B. Nitzsche, M. Ruer, J. Stamford, M. Winzi, R. Heinkel, M. Roder, J. Finell, H. Hantsch, S. J. Jones, M. Jones, F. Piano, K. C. Gunsalus, K. Oegema, P. Gonczy, A. Coulson, A. A. Hyman and C. J. Echeverri, *Nature*, 2005, **434**, 462–469.
25 A. C. Gavin, P. Aloy, P. Grandi, R. Krause, M. Boesche, M. Marzioch, C. Rau, L. J. Jensen, S. Bastuck, B. Dumpelfeld, A. Edelmann, M. A. Heurtier, V. Hoffman, C. Hoefert, K. Klein, M. Hudak, A. M. Michon, M. Schelder, M. Schirle, M. Remor, T. Rudi, S. Hooper, A. Bauer, T. Bouwmeester, G. Casari, G. Drewes, G. Neubauer, J. M. Rick, B. Kuster, P. Bork, R. B. Russell and G. Superti-Furga, *Nature*, 2006, **440**, 631–636.
26 C. Bakal, J. Aach, G. Church and N. Perrimon, *Science*, 2007, **316**, 1753–1756.
27 M. Schuldiner, S. R. Collins, N. J. Thompson, V. Denic, A. Bhamidipati, T. Punna, J. Ihmels, B. Andrews, C. Boone, J. F. Greenblatt, J. S. Weissman and N. J. Krogan, *Cell (Cambridge, Mass.)*, 2005, **123**, 507–519.
28 C. Bakal, *Briefings Funct. Genomics*, 2011, **10**, 197–205.
29 C. Bakal, R. Linding, F. Llense, E. Heffern, E. Martin-Blanco, T. Pawson and N. Perrimon, *Science*, 2008, **322**, 453–456.
30 E. Owusu-Ansah, A. Yavari, S. Mandal and U. Banerjee, *Nat. Genet.*, 2008, **40**, 356.
31 R. Geisler, A. Bergmann, Y. Hiromi and C. Nusslein-Volhard, *Cell (Cambridge, Mass.)*, 1992, **71**, 613–621.
32 P. A. Baeuerle and D. Baltimore, *Science*, 1988, **242**, 540–546.
33 A. A. Beg, T. S. Finco, P. V. Nantermet and A. S. Baldwin Jr, *Mol. Cell. Biol.*, 1993, **13**, 3301–3310.
34 J. Zeitlinger, R. P. Zinzen, A. Stark, M. Kellis, H. Zhang, R. A. Young and M. Levine, *Genes Dev.*, 2007, **21**, 385–390.
35 T. Sandmann, L. J. Jensen, J. S. Jakobsen, M. M. Karzynski, M. P. Eichenlaub, P. Bork and E. E. Furlong, *Dev. Cell*, 2006, **10**, 797–807.
36 T. Sandmann, C. Girardot, M. Brehme, W. Tongprasit, V. Stolc and E. E. Furlong, *Genes Dev.*, 2007, **21**, 436–449.
37 S. M. Gorski, S. Chittaranjan, E. D. Pleasance, J. D. Freeman, C. L. Anderson, R. J. Varhol, S. M. Coughlin, S. D. Zuyderduyn, S. J. Jones and M. A. Marra, *Curr. Biol.*, 2003, **13**, 358–363.
38 J. D. Malhotra, H. Miao, K. Zhang, A. Wolfson, S. Pennathur, S. W. Pipe and R. J. Kaufman, *Proc. Natl. Acad. Sci. U. S. A.*, 2008, **105**, 18525–18530.
39 X. Xue, J. H. Piao, A. Nakajima, S. Sakon-Komazawa, Y. Kojima, K. Mori, H. Yagita, K. Okumura, H. Harding and H. Nakano, *J. Biol. Chem.*, 2005, **280**, 33917–33925.
40 E. F. Blommaart, J. J. Luiken, P. J. Blommaart, G. M. van Woerkom and A. J. Meijer, *J. Biol. Chem.*, 1995, **270**, 2320–2326.
41 T. Noda and Y. Ohsumi, *J. Biol. Chem.*, 1998, **273**, 3963–3966.
42 S. Muratoglu, B. Hough, S. T. Mon and N. Fossett, *Dev. Biol.*, 2007, **311**, 636–649.
43 T. Ideker and N. J. Krogan, *Mol. Syst. Biol.*, 2012, **8**, 565.
44 S. Bandyopadhyay, M. Mehta, D. Kuo, M. K. Sung, R. Chuang, E. J. Jaehnig, B. Bodenmiller, K. Licon, W. Copeland, M. Shales, D. Fiedler, J. Dutkowski, A. Guenole, H. van Attikum, K. M. Shokat, R. D. Kolodner, W. K. Huh, R. Aebersold, M. C. Keogh, N. J. Krogan and T. Ideker, *Science*, 2010, **330**, 1385–1389.
45 C. Baril, M. Sahmi, D. Ashton-Beaucage, B. Stronach and M. Therrien, *Genetics*, 2009, **181**, 567–579.
46 G. Kroemer, G. Marino and B. Levine, *Mol. Cell*, 2010, **40**, 280–293.
47 Y. C. Hou, S. Chittaranjan, S. G. Barbosa, K. McCall and S. M. Gorski, *J. Cell Biol.*, 2008, **182**, 1127–1139.
48 T. E. Rusten, K. Lindmo, G. Juhasz, M. Sass, P. O. Seglen, A. Brech and H. Stenmark, *Dev. Cell*, 2004, **7**, 179–192.
49 D. Ron and P. Walter, *Nat. Rev. Mol. Cell Biol.*, 2007, **8**, 519–529.
50 F. Urano, X. Wang, A. Bertolotti, Y. Zhang, P. Chung, H. P. Harding and D. Ron, *Science*, 2000, **287**, 664–666.
51 I. Tabas and D. Ron, *Nat. Cell Biol.*, 2011, **13**, 184–190.
52 N. Ramadan, I. Flockhart, M. Booker, N. Perrimon and B. Mathey-Prevot, *Nat. Protocols*, 2007, **2**, 2245–2264.
53 K. Zhang and R. J. Kaufman, *Nature*, 2008, **454**, 455–462.
54 P. Walter and D. Ron, *Science*, 2011, **334**, 1081–1086.
55 J. D. Malhotra and R. J. Kaufman, *Antioxid. Redox Signaling*, 2007, **9**, 2277–2293.